Proceedings of the 10th World Congress on Mechanical, Chemical, and Material Engineering (MCM'24)
Barcelona, Spain –August 22-24, 2024
Paper No. HTFF 271
DOI: 10.11159/htff24.271

Effect Of Geometrical Configuration On Cavity Dynamics In Planar Cavitating Venturis

Anuja Vijayan[1], Pradeep Kumar P[1]
[1]Department of Aerospace Engineering,
Indian Institute of Space Science and Technology,
Valiamala, Kerala, India, 695547
anujavijayan.14@res.iist.ac.in; pradeepkumarp@iist.ac.in

Abstract **-** The nature and the dynamics of the cavitation zone in a cavitating venturi are of interest to researchers for correctly predicting the venturi performance under varied operating conditions. The current work presents the influence of the throat configuration and low divergence angle on the cavity dynamics in planar cavitating venturis. The work presents results from Discrete Fourier Transform (DFT) and Spectral Proper Orthogonal Decomposition (SPOD) applied on shadowgraphy images from quasi-steady experiments. In the current work, we have used four planar venturis with different divergent half-angles and throat configurations for the study. Quasi-steady experiments have been conducted for a Pr range of 0.21 to 0.95 and an inlet Reynolds number range of 7.3×10^4 to 2.18×10^5. In our earlier work using 8° (divergent half-angle) venturi, three different frequency behaviours at different pressure ratios (Pr, the ratio of absolute back pressure to inlet pressure) were experimentally observed. The cavitation zone showed low frequency oscillations (corresponding to partial shedding) at high Pr, a mix of low and high frequency oscillations at intermediate Pr and high frequency oscillations (corresponding to cloud cavitation) at low Pr. This venturi has been considered as the reference case for the present studies. The experimental observations show that the geometrical parameters significantly alter the cavity dynamics. The present experiments using a 3° (divergence-half angle) planar venturi showed only low frequency oscillations induced by partial shedding. The experimental evidence from the other two planar venturis shows that the throat configuration (length and width of the throat) also significantly alters the cavity dynamics. For this study, two planar venturis with the same divergence angle but different throat configurations as the reference venturi have been used. An increase in the throat width in one venturi and a reduction in the throat length in the second venturi is observed to promote high frequency cloud shedding behaviour. Increasing throat width and decreasing throat length shifts the mix frequency regime towards high Pr (compared with the reference case). In the first venturi with no finite throat length, the low frequency oscillations are absent. The difference in the cavity dynamics can be attributed to the reduced boundary layer effects due to the reduced throat length.

Keywords**:** Cavitating venturi, cavity dynamics, frequency of oscillations

1. Introduction

Cavitating venturi is a hydrodynamic device that uses the two-phase flow field generated by cavitation to anchor the mass flow rate against a varying downstream pressure. The presence of a two-phase flow, which reduces the sonic speed and creates a choked flow at its throat, is responsible for the flow anchoring property of the venturi. The passive nature of flow control and the absence of moving parts make the device an attractive tool for flow rate control applications. The flow control feature of the cavitating venturi has been well studied by many researchers [1,2], to cite a few, since its inception by L.N. Randall [3]. However, the inter-phase interactions compounded by the turbulence and the multiple scales involved [4] impart difficulties in understanding the physics and modelling the flow field.

The cavitation zone in the venturi primarily has an oscillatory nature [5]. Researchers have broadly understood that *re-entrant jet* (REJ) mechanism [6] and *bubbly shock* [7] are the two dominant mechanisms triggering the cavity dynamics. The cavitation initiation happens near the wall with a bulk flow existing as a liquid core near the venturi axis. The bulk flow impinging on the wall at the cavity termination region (cavity closure) splits into two streams. One stream moves downstream along with the bulk flow. The second stream that moves upstream beneath the cavity, causing partial or complete cloud shedding (based on whether the cavity is thin or thick [6]), is called the re-entrant jet. The adverse pressure gradient in the cavitation zone has been identified as a major cause of the REJ [6]. Typically, while travelling downstream (in the divergent section), the shed cloud will undergo bubble collapses, generating pressure waves (cloud collapse-induced shock waves) that can travel upstream. Upon interaction with the attached cavity, these pressure waves can cause secondary collapses and trigger fresh REJs [7]. However, the bubble collapses occurring at the cavity termination region in the pressure recovery section can also initiate a chain of secondary bubble collapses that can progress upstream as a

condensation void front (condensation shock wave) [8]). Once a cavity is shed, a new cavity grows in its place, the shedding mechanism(s) sets in, and the process is cyclically repeated. The dominance of different mechanisms is influenced by the geometry, the operating conditions, and the thermal effects associated with the working fluid. The surface roughness characteristics, the throat rounding, and the nucleation effects also influence the dynamics. For a comprehensive review of the existing literature in cavitating venturi, the reader is referred to [9]. These different studies provide pointers to the influence of the geometry and the operating conditions on the cavity dynamics.

In the literature, works that report the characterization of cavitating venturi performance in its entire operable regime [10,11,12] under different geometric configurations [2,13] are rare. In our recent study, we have characterized the cavitating venturi operation for the entire range of operating conditions with different divergence half-angles (6°, 8°, and 10°) [14]. The experiments revealed that the cavity dynamics is governed by the REJ at high σ (cavitation number (σ, defined as $\sigma = \frac{P_{out} - P_v}{\frac{1}{2}\rho_l V_{th}^2}$ where P_v is the vapour pressure, P_{out} is the downstream pressure, ρ_l is the liquid density, and V_{th} is the throat velocity) and a combined action of REJ and collapse-induced shock at low σ. The frequency response showed a shift in behaviour from low frequency to high frequency oscillations, based on which the venturi behaviour had been characterized into three different regions: R1, R2, and R3. Region R1 primarily reflects the coupled influence of the low-frequency global oscillation of the cavity and partial shedding. R3 is a region characterized by high frequency cloud shedding due to the combined action of the REJ and the collapse-induced shock wave. Region R2 is influenced by both low and high frequency components. The frequency response featured in the study showed frequency transitions similar to that reported by other investigators [15,16,17]. However, the frequency response reported by Ganesh et al. [8] and Jahangir et al. [11] showed monotonously decreasing frequencies with a reduction in cavitation number. The influence of geometric configuration was proposed to be one of the contributors to the observed differences.

The current work presents the specific aspects of the influence of the throat configuration and the possible limiting behaviour at a low divergent angle. We have used data from four planar venturis (V7, V9, V10 and V11) with different divergent half-angles (V7, V10 and V11 with 8° and V9 with 3°) and throat configurations (V7 and V9 with throat length L_{th}=5 mm, throat width D_{th}=5 mm, V10 with L_{th}=0, D_{th}=5 mm and V11 with L_{th}=5 mm, D_{th}=10 mm) for the study. All these venturis have the same inlet dimension (20mm × 10mm), depth (10 mm) and convergent half-angle (15°). Considering the planar cavitating venturi V7 (8° divergent half-angle, 5mm throat length and 5mm throat width) as our reference case [14], in the current work, the cavity behaviour is experimentally characterized with three different venturis configurations - venturi V9 with a lower divergence half-angle (3°), venturi V10 with a reduced throat length (L_{th}=0) and venturi V11 with an increased throat width (D_{th}=10 mm). We present the influence of these geometric parameters on the dynamic behaviour of the venturi in view of its operation in three distinct regions: R1, R2, and R3. The shadowgraph images obtained from high-speed imaging have been used for analyses using SPOD, DFT, and space-time (x-t) diagrams to assess the different dynamic behaviours.

2. Experimental Methodology

The experimental setup [14] consists of a 200 L stainless steel pressure vessel (water tank pressurized using compressed air), an Alicat pressure controller to set the upstream pressure, an Emerson Coriolis mass flow meter, and a flow control valve at the venturi upstream. Quasi-steady experiments are performed for the entire operable range of the venturis by setting a controlled value of the upstream pressure (such that the fall in the upstream pressure is < 2% during the data logging time) and opening the flow control valve upstream of the venturi. The venturi section is illuminated from the backside using a 1 kW Impex halogen lamp. Shadowgraphy combined with high-speed imaging at a frame rate of 15000 fps and 1280 × 296-pixel resolution is used. Data is recorded using a data acquisition system (Agilent 34980A voltage card) for 3 seconds, during which the Phantom VEO 410L high-speed camera captures and records the instantaneous images for 1 second. Figure 1 is the sketch of the venturi showing the dimensions (not to scale). All the test sections are 400mm long, with a straight inlet section of length 150mm. The cavitation number σ or equivalently pressure ratio Pr denotes the cavitation intensity in the divergent section. A high value of σ or Pr corresponds to low cavitation intensity, and a low value σ or Pr corresponds to high cavitation intensity. The experiments are conducted for a Pr range from 0.21 to 0.95 (±0.66%) and inlet Reynolds numbers (Re_{in}) from 7.3×10^4 to 2.18×10^5 (±0.37%) and upstream pressures from 1.12 to 2.83 bar (±0.62%). The uncertainties reported here are obtained from a systematic uncertainty characterization

[14,18]. The following subsection, 2.1, briefly discusses the different methodologies adopted in the current work. A detailed description of the experimental setup, procedure, the methodology adopted for image processing, the data reduction techniques, and the sufficiency of the various methods are presented in [14,18].

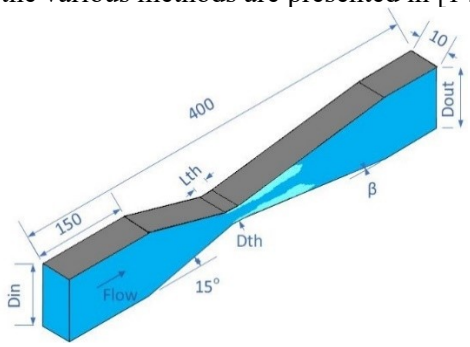

Fig. 1: Sketch of the venturi (All dimensions are in mm; β – divergent half-angle).

2.1. Image Processing

The image processing, Fourier decomposition, and SPOD algorithms are implemented in MATLAB to obtain the time-averaged cavity lengths, the cavity oscillation frequencies, and the mode shapes.

***Cavitation zone length*:** The distance from the throat entrance to the cavitation termination is defined as the cavitation zone length. The images are corrected (for minor light intensity variations by negating from a background image) and cropped appropriately. Fifteen thousand images are grouped into five bins, each containing 3000 images (bin size decided based on the correlation coefficients of the mean and standard deviation images [18], and the cavity length is obtained by averaging the lengths obtained from individual bins. In line with the literature [1], the camera is positioned to ensure minimum brightness-fall towards the edge of an image. In the present experiments, the viewing window length is 90-175 mm, the working distance is 600-950 mm, and the maximum possible intensity fall-off error is within 2.6% for this arrangement. This error is further reduced by arranging the cavitation zone in the middle of the viewing window.

Cavity oscillation frequency: The DFT and SPOD algorithms use pixel intensities from the images to find the temporal and the spatio-temporal flow components. For DFT frequencies, 15000 images are grouped into nine bins (with an overlap of 50%), each containing 3000 images. A rectangular region of length 100 pixels and width equal to the venturi width is selected at the cavity termination, and the sum of the pixel intensity values is used for obtaining the one-sided frequency spectrum from DFT. The final frequency value reported is the average value obtained from the nine bins.

Spectral Proper Orthogonal Decomposition: Spatially dominant patterns and their temporal evolution are extracted using SPOD, which gives optimum orthogonal modes. SPOD gives spatially and temporally coherent structures. In the present work, every alternate snapshot (to get a frequency resolution of ±15 Hz) from 0 to 10752 is arranged into 20 blocks (to get 20 modes), each with 512 images and 50% overlap between blocks. A typical energy spectrum from SPOD analysis is shown in figure 2. The first mode of the first and second dominant frequency bin contains 94.9% and 90.3% energy, respectively, for this data point. Figure 3 is a typical plot showing the energy content of the different modes in venturi V11. The % energy contribution of the dominant mode depends on the geometry and the operating conditions; the % energy content of the first mode is greater than 80% for venturi V10 and V11. (The percentage energy contribution of the primary frequencies in V9 is less than 60%, mainly because of the lower amplitude of cavity oscillations.)

Space-time diagrams: Space-time (x-t) diagrams are obtained by averaging each image in the flow-perpendicular direction and stacking the resulting vectors on the time axis. This type of diagram is a complementary tool in identifying the various oscillatory mechanisms and their transitions under different geometry and operating conditions.

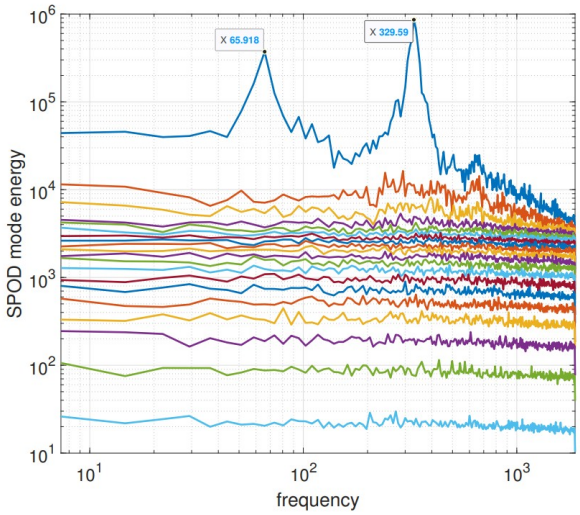

Fig. 2: SPOD energy spectrum for venturi V10 at Pr=0.734.

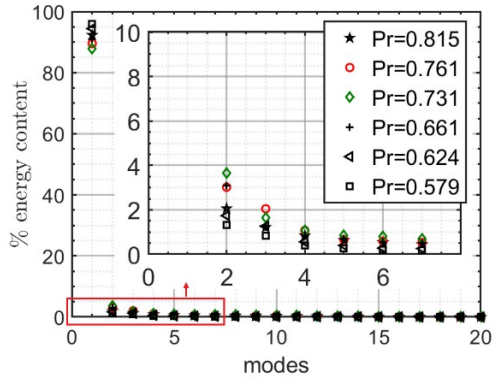

Fig. 3: % energy contribution of different modes at various pressure ratios for venturi V11.

3. Results and Discussion

3.1. Influence of the Divergence Angle on Cavity Length and Dynamics

Figure 4 shows the cavity length in the 3° venturi V9 compared with that in V7 (8°) from the previous study [14]. The figure shows that under similar operating conditions, the cavity length in a venturi with a lower divergent angle will be much higher than in a venturi with a higher divergent angle. When the divergent angle reduces, the flow will be more attached to the wall because of the reduced losses and the reduced flow separation. Therefore, as expected, the cavity length at the same pressure ratio is greater for the 3° venturi (V9) than for V7 (Figure 4). Typically, the cavity length versus the pressure ratio plot shows increased sensitivity to the external pressure perturbations [9,14] below a transition pressure ratio (Pr_{tr}). This transition (presented in table 1) can be found from a regression analysis performed on the length data. As evident from figure 4, there is no transition point for venturi V9. As we will see later, the transition happens not at a point but over a region. The absence of Pr_{tr} in V9 can be directly related to its dynamic behaviour.

Figure 5 shows the DFT frequencies presented in terms of the non-dimensional Strouhal number and the cavitation number for different venturis. The Strouhal number is the oscillation frequency non-dimensionalised with a characteristic length scale and velocity scale. Generally, any suitable length and velocity scale can be used to non-dimensionalise the frequency. However, the statistically averaged attached cavity length is the best representation of the cavitation extent at a particular operating condition. Similarly, the average throat velocity best represents the characteristic velocity at a given operating condition with the additional advantage of being easily quantifiable from flow rate measurements. Therefore, in the present work, the Strouhal number St_{Lcv} is defined as $St_{Lcv} = L_{cv} f / V_{th}$, where L_{cv} is the cavity length, f is the frequency,

and V_{th} is the throat velocity. Though this definition is not universal, it is chosen considering the recommendation of Dular et al. [19] for hydrofoil geometries.

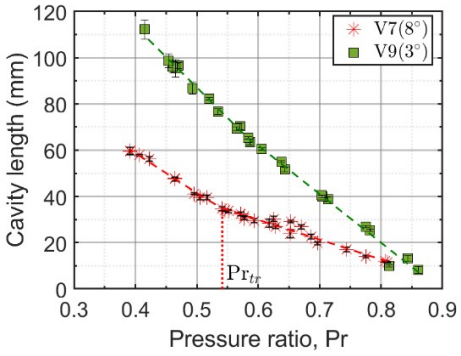

Fig. 4: Cavity length in V7 and V9; dashed lines are fitted using regression analysis. Data for V7 is from [14].

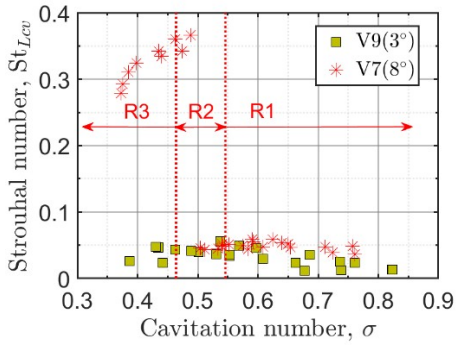

Fig. 5: St_{Lcv} versus σ for V7 and V9. Regions R1, R2 and R3 for V7 are also marked. Data for V7 is from [14].

As discussed in section 1, our previous work [14] using 6°, 8 ° and 10 ° planar venturis presented the cavitation behaviour in planar venturis categorized into three regions. Region R1 is characterized by low frequency global oscillations of the attached cavity (a large-scale oscillation in the length of the attached cavity without considerable cloud shedding), and region R3 is characterized by high frequency cavity oscillations associated with the cloud cavitation due to the combined effect of REJ and collapse-induced shock. The collapse-induced shock waves were observed to trigger new REJs. There is an overlap transition region R2 where the low frequency and high frequency components co-exist (figure 5). The span of the transition region was found to be decreasing with the increasing divergence angle. The increased flow separations, aiding more energetic re-entrant jets, could be ascribed as the cause of this behaviour. The present results indeed agree with the previous proposition; for very low β (3° venturi V9 in figure 5), the influence of cloud shedding becomes vanishingly small, and the entire cavitation behaviour can be characterized by region R1 alone. The x-t diagram in figure 6 proves that the cavitation zone in V9 shows only small-scale tail-end partial shedding (shown using a yellow arrow named B in the figure). However, the attached cavity has no evident global length oscillation (unlike in venturi V7 [14]). This partial shedding (due to a small re-circulation at the cavity closure) is not energetic enough to trigger fresh REJs. The x-t plot shown in figure 6 is further evidence for the absence of shock-wave triggered REJ even at the lowest Pr value of 0.415 in V9. Since the present geometry, V9, has a low divergent angle, the REJ may not be aided by the high adverse pressure gradient in the pressure recovery zone. The instantaneous, time-stacked raw images for Pr=0.415 shown in figure 7 provide further proof for the absence of large-scale length oscillation in V9. The cavity termination region does not change much, as the figure shows. A small-scale re-circulation (shown by a curved yellow arrow) is observed in figure 7a, which causes partial tail-end shedding (yellow dashed circles). As stated earlier, this tail-end shedding, which happens throughout the data-acquiring time, is not observed to trigger REJs or cause large-scale cavity length oscillations.

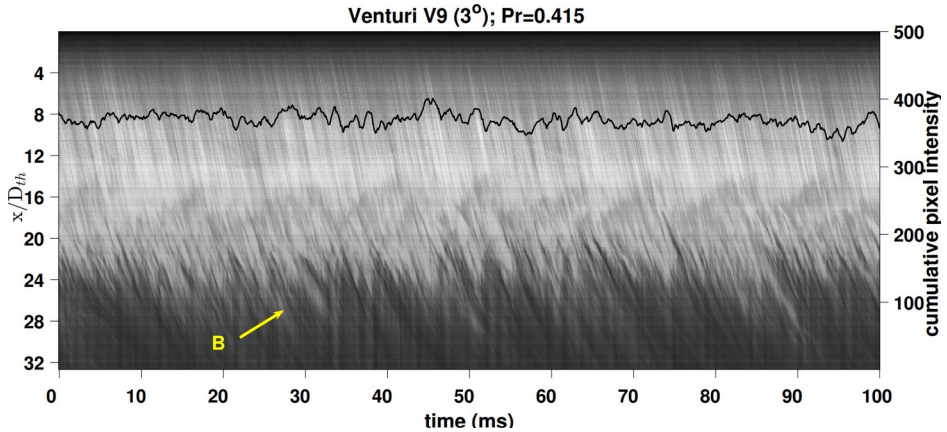

Fig. 6: x-t diagram for venturi V9 at Pr=0.415. The solid black lines are cumulative pixel intensities. Yellow arrow marked B - small-scale shedding at the cavity tail end.

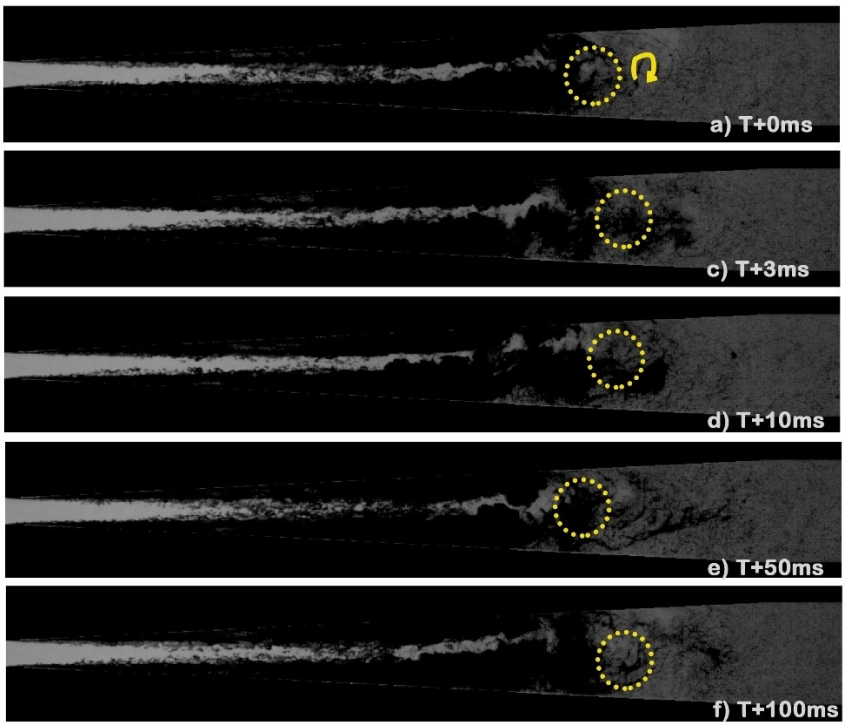

Fig. 7: Instantaneous images for V9 at Pr=0.415. Yellow arrows - small re-circulation at tail end; yellow dashed circle - tail-end shedding

Figure 8 shows the energy spectrum (% energy content) of the SPOD modes for venturi V9 at its lowest cavitation number (σ=0.387, Pr=0.415). The spectrum shows the prominence of low frequency modes. However, even at the lowest Pr, the first mode of the fundamental frequency is less distinguishable from other modes (contributing only 57.6% of the total energy content of all modes), contrary to its nature and appearance in higher divergent angles (figure 2). All the evidence presented in figures 5-8 confirms that the venturi shows only R1 behaviour.

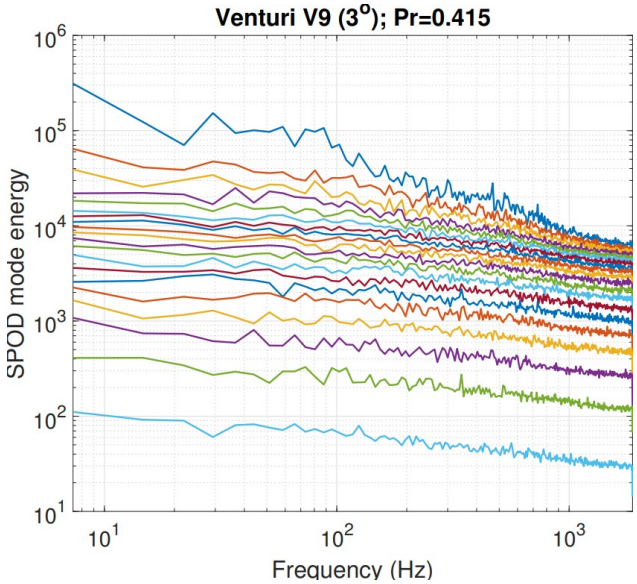

Fig. 8: SPOD percentage energy spectrum (showing prominence of low frequency modes) for venturi V9 at Pr=0.415.

3.2. Influence of the Throat Configuration on Cavity Dynamics

As discussed in Section 1, the variation in geometry, especially the throat configuration, could influence the cavity dynamics. The investigations by Ullas et al. [13] and Dular et al. [20] under limited operating conditions provide pointers to the influence of throat configuration on cavity dynamics. In the current work, we experimentally investigate the effect of throat configuration on the cavity dynamics using two venturis V10 (L_{th}=0, D_{th}=5 mm, β=8°) and V11 (L_{th}=5 mm, D_{th}=10 mm, β=8°) for the entire operable range of the venturis. As before, Venturi V7 (L_{th}=5 mm, D_{th}=5 mm, β=8°) is considered as the reference venturi. In line with our previous study [14], V10 and V11 also show a transition in oscillation frequency from low frequency to high frequency with an overlap region in between. A systematic frequency analysis performed on two image patches of area, 2 mm^2 each, taken from the inlet and throat of the venturi section, showed no signatures of inlet flow disturbances (system instabilities [6]). The extracted cavity oscillation behaviour in regions R1, R2, and R3 are shown in figure 9 using frequencies obtained from DFT.

It is observed from figure 9 and table 1 that the transition region is at $0.733 \leq Pr \leq 0.843$ for venturi V10 when compared to the transition region at $0.464 \leq Pr \leq 0.546$ in V7. Interestingly, there is an observable shift of region R2 towards high Pr and a visible change in its span. Additionally, in venturi V10, region R1 is almost absent. Figure 10 shows an x-t plot for two cases, one in region R2 and another in region R3, in venturi V10. The light region in the figure corresponds to the vapour zone, and the dark region corresponds to the liquid zone. At a high pressure ratio (Pr=0.734, σ=0.656 in the top palette of figure 10), there is a low frequency global oscillation of the attached cavity, which cause an overall oscillation in cavity length (marked as A). Dark streaks of lines (marked using yellow dotted arrows named C) in the x-t plot denote the sudden appearance of liquid (cloud collapse and associated sudden vapour condensation due to the collapse-induced shock). At Pr=0.734, both the low and the high frequency components co-exist, causing the venturi to show R2 behaviour. When the Pr reduces (Pr=0.482, σ=0.422 in the bottom palette of figure 10), the frequency will be more dominated by the high frequency oscillations. Dark streaks (dotted yellow arrow marked C) appear in all cycles of cavity growth and shedding. These collapse-induced shock waves on meeting the cavity will trigger REJs (solid blue arrows marked R), which will pinch off the cavity while progressing upstream, thereby causing downstream vapour convection (cloud shedding marked using dashed black arrows named V in figure 10). In the pressure recovery zone, the shed clouds collapse and trigger fresh REJs; meanwhile, the attached cavity re-grows (marked using violet solid arrows named G).

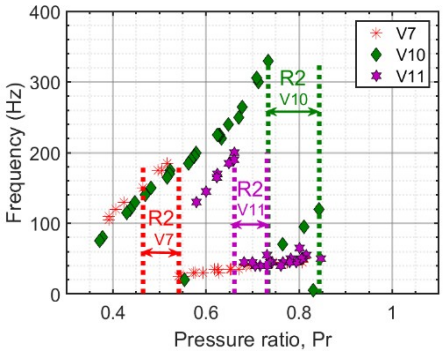

Fig. 9: Transition region in V10 (marked R2 V10) and V11 (marked R2 V11) compared with that in V7.

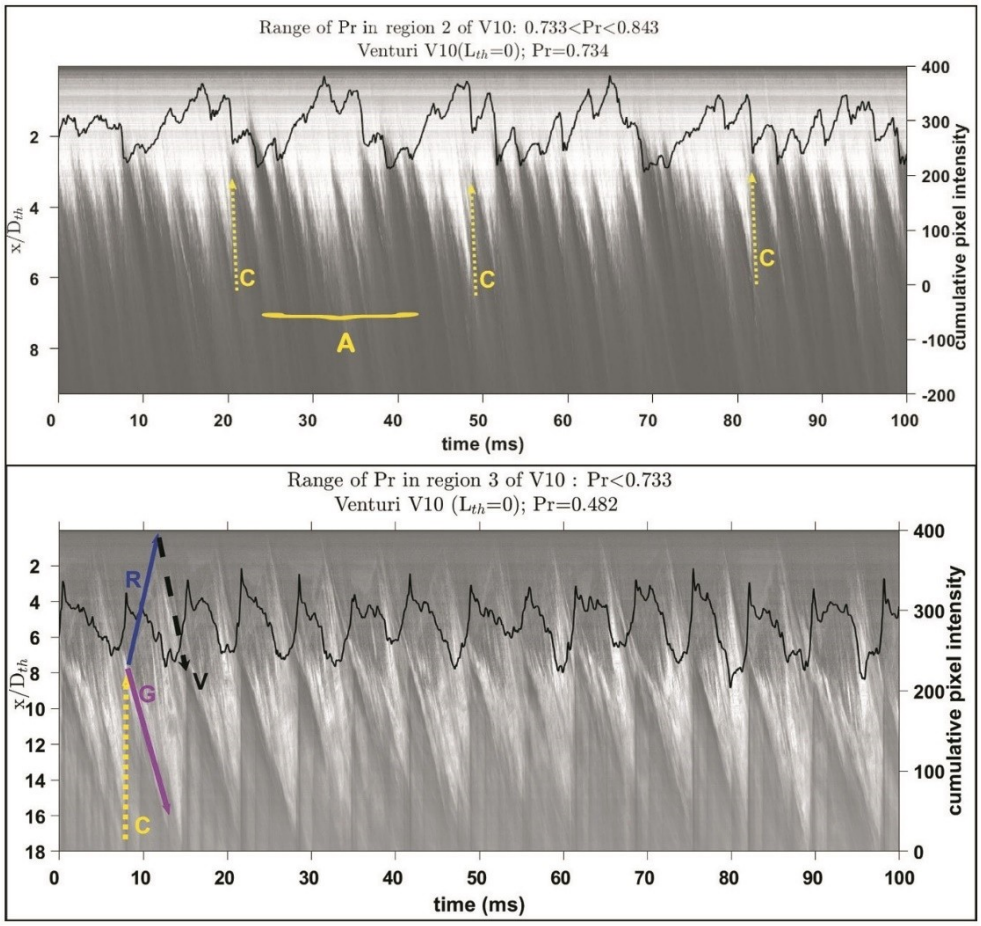

Fig. 10: Typical x-t plots for region R2 and region R3 in V10. The solid lines are cumulative pixel intensities. Yellow brace named A - global cavity length oscillation; yellow dotted arrows named C - cloud collapse; violet solid arrow named G - cavity growth; blue solid arrow named R - REJ; black dashed arrow named V - vapour convection.

Figure 11 shows the instantaneous images for venturi V10 at Pr=0.482. In figure 11a, the remnants of the cloud shed in the previous cycle are seen (marked using a yellow dashed circle). The cloud shedding triggers REJ (white arrow) that progresses upstream (white dashed circles in figure 11b-d) and causes swelling of the cavities (green dashed circles). As time progresses, the REJ reaches the throat, causing cavity swelling, as shown in figure 11d. The swollen cavities are eventually shed and undergo a chain of events, including the fusion of the small cavities, circulation of the cavity, and

collapse. The collapse phase triggers fresh REJ. In this venturi, the REJs are seen traversing up to the throat. The upstream progression of REJ till the venturi throat is contrary to its behaviour in V7, where the REJ does not reach the throat [14].

Table 1: Transition pressure ratios in different venturis

Venturi	Transition Pr range from DFT	Transition Pr from regression analysis
V7	0.546 – 0.464	0.542
V10	0.843 – 0.733	0.765
V11	0.731– 0.661	0.682

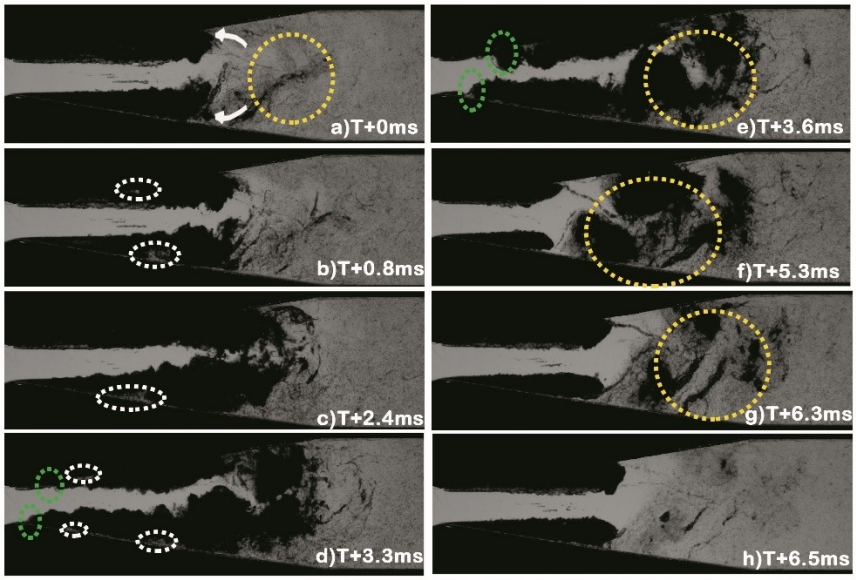

Fig. 11: Instantaneous images stacked time-wise for venturi V10. White arrows - REJ; yellow dashed circle - cavity cloud; white dashed cloud - REJ progressing upstream; green dashed circle - swelling of the cavity due to REJ motion underneath it.

Recent studies, both experimental [21] and numerical [13], show that a definite throat length increases the extent of the boundary layer compared to a venturi without throat length. In the absence of the throat length, as in venturi V10, the boundary layer is expected to be thin, and the reduced wall shear will, in turn, promote the easier formation of strong re-entrant jets. Moreover, the absence of the throat length causes a sudden change in the course of the streamlines at the throat, thereby enhancing the flow separation. Consequently, the REJ possibly encounters lower resistance in its progression upstream and hence is observed to be progressing upstream till the throat (shown in figure 11d). Thus, in the absence of the throat, the REJ can easily reach the throat, causing large-scale cloud shedding. The dominant frequencies of the cloud shedding are similar for V7 (Lth= 5 mm) and V10 (Lth= 0). However, the dominant frequency of the attached cavity oscillation is one order higher than that in V7, possibly because of the easy formation and propagation of the re-entrant jet.

The frequency response of venturi V11 (of higher throat width compared to reference venturi) is shown in figure 9. Similar to the behaviour of V10, there is a visible shift of region R2 towards a high Pr range in venturi V11. It is observed that the behaviour easily transitions to R3. This venturi shows the transition region R2 at $0.661 \leq Pr \leq 0.731$. The effective throat width in a venturi of a small throat will still be smaller because of the boundary layer effects at the top and the bottom converging-diverging sections. Conversely, when the throat width increases, the boundary layer effects reduce, and the flow can easily transition to a cloud cavitation regime because of the easier upstream propagation of the REJ. Figure 9 also shows that the venturi dynamics in V10 and V11 have a longer span of R3 behaviour, which means that the venturi can easily transition to a cloud cavitation regime. Further, an increase in the throat width shows a reduction in the dominant cloud shedding frequency, as evident from figure 9, possibly because of the reduced interaction of the upper and lower cavity lobes. Consequently, the Strouhal number (St_{Lcv} in figure 12) also exceeds the range reported in our previous study

[14]. These results indicate that the throat configuration can significantly affect the nature and dynamics of the cavity in internal cavitating flows.

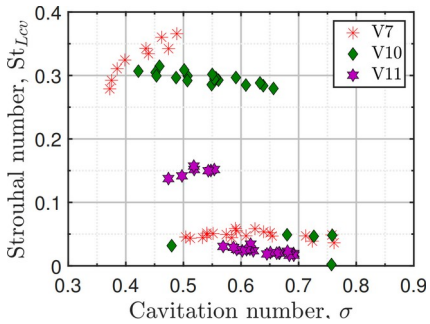

Fig. 12: St_{Lcv} for V10 and V11 compared to that of V7.

As observed in our previous studies [14], the frequency response shown by our planar venturi geometries was different from the frequency trends reported by the planar geometries of Ganesh et al. [8] and Wu et al. [22] and the axisymmetric geometry of Jahangir et al. [11]. The observed differences could be ascribed to the increased interactions between the upper and the lower cavity lobes (due to the smaller throat width) and the increased boundary layer thickness (due to a definite throat length). However, the frequency response in the cloud cavitation regime in the present geometries is similar to the frequency response reported by Ganesh et al. [8], Jahangir et al. [11] and Wu et al. [22]. Therefore, as the throat length reduces and the throat width increases, the venturi could have an easy transition to the behaviour shown by the venturi geometries of Ganesh et al. [8] and Jahangir et al. [11].

4. Conclusions

An experimental study of the influence of the divergent angle and the venturi throat configuration on the nature and dynamics of the cavitation zone in planar cavitating venturi is presented in this work. We have used three planar venturis with different divergent half-angles (V9 with 3° and V10 and V11 with 8°) and throat configurations (V9 with L_{th}=5mm, D_{th}=5 mm, V10 with L_{th}=0, D_{th}=5 mm and V11 with L_{th}=5 mm, D_{th}=10 mm) for the study. Quasi-steady experiments have been conducted for a Pr range of 0.21 to 0.95 and an inlet Reynolds number range of 7.3×104 to 2.18×105. High-speed shadowgraphy images have been used to decipher the dynamics in the flow field. The observations reported in the present study show that the geometrical parameters do significantly alter the cavity dynamics. The dynamic behaviour of venturis of higher divergence angle can be categorised into three regions: R1 (low frequency region), R2 (mix of low and high frequency region) and R3 (high frequency region). When the divergent angle is very small, the behaviour of the venturi is entirely characterised by low frequency oscillations (R1) corresponding to small-scale tail-end shedding at the cavity termination region. The throat configuration significantly influences the cavity dynamics. An increase in throat width and a decrease in throat length shifts the transition region (R2) towards high Pr and pushes the cavity dynamics into a larger span of cloud cavitation regime (R3). In the venturi with no finite throat length, the cavity behaviour shifts to regions R2 and R3 with an absence of region R1. The difference in the cavity dynamics can be attributed to the reduced boundary layer effects due to the reduced throat length. To conclude, the work presented in this paper significantly adds a plethora of information to the existing knowledge about cavitating venturi by characterising the cavity dynamics in planar venturis under varied geometrical configurations, such as a small divergence angle and changed throat configurations.

Acknowledgements

We express our sincere gratitude to Dr Sunil Kumar S., Deputy Director, PRS, LPSC, ISRO, for the valuable comments and suggestions and the fruitful discussions regarding the operation of cavitating venturi in their test facility. We would like to thank the scientists and staff of TCF, and PRS, LPSC, ISRO for providing the manufacturing facility and accessories for the experimental setup. We thank Mr. Dinesh D. and Mr. Bipin Davidson of Thermal and Propulsion Lab, Indian Institute of Space Science and Technology, for their assistance in the smooth conduct of the experiments.

References

[1] A.M. Abdulaziz, "Performance and image analysis of a cavitating process in a small type venturi," *Exp. Therm. Fluid Sci*., vol. 53, pp. 40-48, 2014.

[2] S.M. Ashrafizadeh and H. Ghassemi, "Experimental and numerical investigation on the performance of small-sized cavitating venturis," *Flow Meas. Instrum.,* vol. 42, pp. 6-15, 2015.

[3] L.N. Randall, "Rocket applications of the cavitating venturi," *J. Am. Rocket Soc*., vol. 22, no. 1, pp. 28-31, 1952.

[4] M. Ishii and T. Hibiki, *Thermo-fluid dynamics of two-phase flow*. Springer Science & Business Media, 2010

[5] K. Sato and S. Shimojo, "Detailed observations on a starting mechanism for shedding of cavitation cloud," in *Proceedings of the 5th International Symposium on Cavitation CAV 2003*, Osaka, Japan, 2003, GS_4_009.

[6] M. Callenaere, J.-P. Franc, J.-M. Michel, and M. Riondet, "The cavitation instability induced by the development of a re-entrant jet," *J. Fluid Mech.*, vol. 444, pp. 223–256, 2001.

[7] Y. Saito and K. Sato, "Bubble collapse propagation and pressure wave at periodic cloud cavitation," in *Proceedings of the 6th International Conference on Multiphase Flow*, ICMF 2007, Leipzig, Germany, July 9–13, 2007, S7_Tue_C_25.

[8] H. Ganesh, S. A. M$\ddot{a}$kiharju, and S. L. Ceccio, "Bubbly shock propagation as a mechanism for sheet-to-cloud transition of partial cavities," *J. Fluid Mech.*, vol. 802, pp. 37–78, 2016.

[9] V. Anuja, P. Pradeep Kumar, "Characterization of cavitation zone in cavitating venturi flows: Challenges and road ahead," *Phy. Fluids*., vol. 35, no. 11, pp. 111301, 2023.

[10] X. Long, J. Zhang, J. Wang, M. Xu, Q. Lyu, and B. Ji, "Experimental investigation of the global cavitation dynamic behavior in a venturi tube with special emphasis on the cavity length variation,"*Int. J. Multiph. Flow*,vol. 89, pp. 290–298, 2017.

[11] S. Jahangir, W. Hogendoorn, and C. Poelma, "Dynamics of partial cavitation in an axisymmetric converging-diverging nozzle," *Int. J. Multiph. Flow*, vol.106, pp. 34–45, 2018.

[12] J. Wang, L. Wang, S. Xu, B. Ji, and X. Long, "Experimental investigation on the cavitation performance in a venturi reactor with special emphasis on the choking flow," *Exp. Therm. Fluid Sci.*, vol. 106, pp. 215–225, 2019.

[13] P. K. Ullas, D. Chatterjee, and S. Vengadesan, "Experimental study on the effect of throat length in the dynamics of internal unsteady cavitating flow," *Phys. Fluids*, vol. 35, 023332, 2023.

[14] V. Anuja and P. Pradeep Kumar, "Experimental characterization of cavitation zone and cavity oscillation mechanism transitions in planar cavitating venturis," *Phy. Fluids*., vol. 35, no. 8, pp. 08331, 2023.

[15] T. Keil, P. F. Pelz, U. Cordes, and G. Ludwig, "Cloud cavitation and cavitation erosion in convergent divergent nozzle," in *Proceedings of the WIMRC 3rd International Cavitation Forum*, University of Warwick, UK, 2011.

[16] A. Danlos, F. Ravelet, O. Coutier-Delgosha, and F. Bakir, "Cavitation regime detection through proper orthogonal decomposition: Dynamics analysis of the sheet cavity on a grooved convergent–divergent nozzle," *Int. J. Heat Fluid Flow*, vol. 47, pp. 9–20, 2014.

[17] K. Croci, P. Tomov, F. Ravelet, A. Danlos, S. Khelladi, and J.-C. Robinet, "Investigation of two mechanisms governing cloud cavitation shedding: Experimental study and numerical highlight," in *ASME 2016 International Mechanical Engineering Congress and Exposition*, Arizona, USA, 2016.

[18] V. Anuja, P. Pradeep Kumar and K. Iyer, "Experimental study and numerical sizing model for cavitation zone characterisation in cavitating venturis," *S$\bar{a}$dhan$\bar{a}$*, vol. 48, no. 82, pp. 1– 16, 2023.

[19] M. Dular and R. Bachert, "The issue of Strouhal number definition in cavitating flow," *J Mech. Eng.*, vol. 55, no. 11, pp. 666–674, 2009.

[20] M. Dular, I. Khlifa, S. Fuzier, M. Adama Maiga, and O. Coutier-Delgosha, "Scale effect on unsteady cloud cavitation," *Exp Fluids*, vol. 53, no. 5, pp. 1233–1250, 2012.

[21] T. Jiang, Z. Huang, J. Li, Y. Zhou, and C. Xiong, "Effect of nozzle geometry on the flow dynamics and resistance inside and outside the cone-straight nozzle," *ACS omega*, vol. 7, no.11, pp. 9652–9665, 2022.

[22] X Wu., E. Maheux, and G.L. Chahine, "An experimental study of sheet to cloud cavitation," *Exp Therm. Fluid Sci.*, vol. 83, pp. 129–140, 2017.